A Generic Voltage Control for Grid-Forming Converters with Improved Power Loop Dynamics

Han Deng, Jingyang Fang, Yang Qi, Yi Tang, Vincent Debusschere

A Generic Voltage Control for Grid-Forming Converters with Improved Power Loop Dynamics

Han Deng, *Student Member, IEEE,* Jingyang Fang, *Member, IEEE,* Yang Qi, *Member, IEEE,* Yi Tang, *Senior Member, IEEE,* and Vincent Debusschere, *Senior Member, IEEE*

***Abstract*—Grid-forming converters (GFMCs) provide voltage support and other grid services, such as inertia and droop, in more-electronics power systems. The GFMCs with small droop coefficients or connected to the grid through a small impedance may have a fast power loop, which leads to serious conflicts with the inner ac voltage control loop, resulting in power oscillations or even instability. To address this problem, an extremely fast ac voltage loop should be expected for GFMCs. On top of that, GFMCs must operate well in both stand-alone and grid-tied conditions. Through detailed analysis, this paper first reveals that the grid-tied operation of a dual loop controlled GFMC with an *LCL* output filter features a much slower voltage control loop than that of the stand-alone mode. To improve the dynamics of GFMCs, we propose a generic voltage control scheme with a high-pass filter in the current feedback loop. The generic voltage controller has fast voltage tracking performances under both grid-tied and stand-alone operations, thereby enabling GFMCs to achieve better power regulation and grid service. The improvements in both voltage tracking and power control are verified via experiments.**

***Index Terms*—Grid-forming converter, *LCL* filter, power control, stability, voltage control.**

I. Introduction

TO reduce the carbon footprint, power electronics device-interfaced distributed generations (DGs) are widely integrated into modern power grids [1]. Conventionally, DGs are coupled to the grid through current vector-controlled voltage source converters (VSCs) with phase-locked loops (PLLs), which are also named as grid-feeding converters (GFDCs) [2]. Although GFDCs have a fast response and can limit current easily, GFDCs cannot provide voltage support, which is necessary in power electronics-dominated power systems. Furthermore, the negative influence of the PLL introduces instability under weak grids [3]. To address these challenges, voltage vector-controlled grid-forming converters (GFMCs) emerge as a new trend [4].

GFMCs use vector voltage control to operate as a stiff ac voltage source. With the same control structure, GFMCs can work regardless of whether they are connected to the grid. The control of GFMCs includes an outer power control loop and an inner voltage control loop. For the power control loop, droop control is applied in parallel-connected UPS systems to achieve autonomous power sharing [5]. The power-synchronization control utilizes the inherent synchronization mechanism in an ac system to synchronize the VSC with the grid [6]. Virtual synchronous generators (VSGs) or virtual synchronverters further simulate the inertia and droop mechanism of synchronous generators to achieve power sharing and grid frequency support [7]. The low-pass-filtered power feedback combined with the droop control is proved to be equivalent with the VSG control in view of the virtual inertia provided to the grid [8]. The dynamic characteristics of different droop mechanism and virtual inertia implementation strategies in GFMCs are evaluated in [9]. The coupling effects of active and reactive control and related stability issues are studied in [10]. [11] analyzes the synchronization stability of GFMCs with capacitors as dc power supplies. [12] investigates the complete small signal models of GFMCs with capacitors and batteries dc sources. To address the low-frequency oscillation problem in microgrids with interconnected GFMCs, a passivity-based design criteria for individual GFMCs is proposed in [13], and a converter-based power system stabilizer is proposed in [14].

Voltage vector linear control strategies have been comprehensively investigated as well. To provide a pure voltage output with small switching harmonics, LC filters are usually employed in VSC applications [15]. For grid-tied applications, the inverter-side LC filter and the grid-side impedance will form an LCL filter. Although LC/LCL filters can effectively suppress switching harmonics with a reduced size, LC/LCL resonances will occur and bring stability issues. Generally, multi-loop control structures are utilized in the LC/LCL systems to achieve reference tracking and stability improvement simultaneously [15]. The principle for inverter-side or capacitor-side current feedback damping is elaborated in [16]–[18]. Capacitor voltage feedback active damping can also contribute to the stability and the waveform quality of LC filtered grid-tied systems [19]–[21]. These active damping methods are widely employed in LC/LCL filtered GFMCs with dual-loop voltage controllers. To reduce sensor cost, [22] utilizes the internal phase lag of the digital controller computation delay and integrator dominant controllers to avoid stability problems without damping when using a single-loop voltage controller. Apart from the stability and power quality concerns, several voltage control schemes with high control bandwidth are evaluated in [23].

When designing the outer power control loop structures and parameters, it is usually assumed that the power is much slower than the inner voltage control loop for simplicity. As a result, the voltage control loop can be regarded as a unit constant. This is a simple and effective approach in the multi-loop controller design.

However, the inner voltage loop of GFMCs is usually designed under the stand-alone mode [18], [23]. This paper reveals that the voltage tracking dynamic response of a dual-loop voltage controlled GFMC under the grid-tied mode is much slower than that under the stand-alone mode. Further-

Part of this paper has been presented at the Energy Conversion Congress and Exposition (ECCE), 2021. This submission is a much extended version.

more, under cases of strong grids with small grid impedance or DGs with small capacities and low droop coefficients, the power loop bandwidths will be high [24]. This means the hypothesis of the control bandwidth decoupling might not stand even when the voltage control loop is designed to be fast under the stand-alone mode. The voltage loop with a slow dynamic response will cause coupling between the outer power control loop and the inner voltage control loop, which may lead to unsatisfied power control dynamics and even instability. To address this issue, a high-pass filtered current feedback method is proposed, which has little influence on the operation of GFMCs under the stand-alone mode. With the proposed controller, GFMCs can achieve fast and stable voltage tracking performance under both stand-alone and grid-tied modes without any controller alternations. More importantly, the power control stability is also improved especially when the power control bandwidth is high.

The rest of the paper is organized as follows. Section II presents dynamic analysis of the voltage control loop under stand-alone and grid-tied modes and reveals the poor voltage tracking dynamic response of GFMCs under the grid-tied mode. Section III introduces the power control loops of GFMCs along with their interaction with the voltage control loops. Section IV proposes a generic voltage controller to improve the voltage tracking dynamics under the grid-tied mode. Section V discusses the similar problem of worsened dynamic responses in other controllers and other possible solutions. Experimental results are provided in Section VI for verification. Finally, Section VII concludes the paper.

II. Dynamic Analysis of Voltage Control Loop

Although lots of research has studied the control of LC filtered voltage controlled VSCs, and several control strategies with fast response have been proposed, most of them considered the scenario when the VSC is disconnected from the grid. When the VSC is connected to the grid, the grid-side current is usually considered as a disturbance to the system when analyzing the voltage loop dynamics.

This section will introduce the schematic of the studied GFMC system firstly, then show that the dynamic responses of the GFMCs will deteriorate when they are connected to the grid with the conventional dual loop control.

A. System Schematic

Fig. 1 shows the general system schematic diagram of a GFMC. The GFMC is connected to the grid through an LC filter composed of L_{i} and C_{f}. L_{g} represents the grid impedance. Note that if an LCL filter is applied, then L_{g} will also include the grid-side inductance of the LCL filter. The dc source v_{dc} can be either a dc voltage source or a capacitor, representing a battery or the output of another converter in a multi-stage system [25].

Generally, the active power P and the reactive power Q flowing from the GFMC to the grid v_{g} can be controlled by tuning the phase reference $\theta_{\mathrm{oref}} = \int \omega_{\mathrm{oref}} dt$ and the amplitude reference V_{oref} of the capacitor voltage v_{o}, where ω_{oref} denotes the output frequency reference of the GFMC. The subscript ref represents the reference signals, abc stand for the three

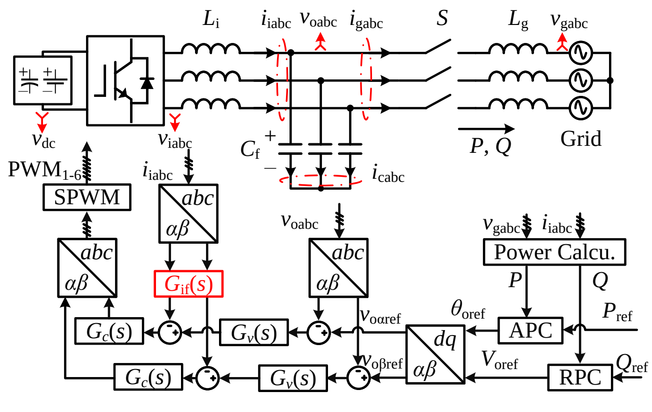

Fig. 1. Topology and control schematic of a GFMC.

phase ac signals, $\alpha\beta$ denote the signals in the stationary quadrature frame after Clarke's transform, and dq represent the signals in the synchronous frame after Park's transformation. The voltage over the capacitor v_{o} can be controlled under either the stationary $\alpha\beta$ frame or the synchronous dq frame, with the controller $G_{\mathrm{v}}(s)$ being a proportional-resonance (PR) controller or a proportional-integral (PI) controller, respectively. The current controller $G_{\mathrm{c}}(s)$ uses a proportional (P) controller, which feeds back the inverter-side current i_{i} to damp the LC resonance [16]. i_{g} and i_{c} represent the grid current and the capacitor current, respectively. The current feedback filter $G_{\mathrm{if}}(s)$ is bypassed in the conventional dual-loop voltage control.

B. Voltage Control Loop Modeling

Fig. 2 demonstrates the control scheme of an LCL-filtered GFMC in the $\alpha\beta$ frame. The solid part represents the stand-alone mode, and the grid-tied mode should include the dotted part. Note that the analysis can be similarly applied for the PI controller in the synchronous dq frame, as the equivalence has been proved in [26]. In the $\alpha\beta$ frame, the voltage controller $G_{\mathrm{v}}(s)$ is usually a proportional resonant (PR) controller, i.e.

$$G_{\mathrm{v}}(s) = K_{\mathrm{vp}} + \frac{2K_{\mathrm{vr}}s}{s^2 + 2\zeta_{\mathrm{r}}\omega_1 s + {\omega_1}^2}, \tag{1}$$

where K_{vp} is the proportional gain, K_{vr} is the resonant gain, and ω_1 is the nominal grid frequency. ζ_{r} is the damping factor of the PR controller, whose value is selected as 0.01 to ensure satisfying tracking performance within the range of of $(1 \pm 0.01)\omega_1$. The current controller $G_{\mathrm{c}}(s)$ is chosen as

$$G_{\mathrm{c}}(s) = K_{\mathrm{cp}}, \tag{2}$$

where K_{cp} is the current loop gain. The computation and PWM is modeled as a delay function, i.e.

$$G_{\mathrm{d}}(s) = e^{-sT_{\mathrm{d}}}, \tag{3}$$

where the delay time is $T_{\mathrm{d}} = 1.5T_{\mathrm{s}}$. $T_{\mathrm{s}} = T_{\mathrm{sw}}$ is the sampling or switching time period. $G_{\mathrm{if}}(s)$ is the current feedback filter, which is a unit gain or bypassed in the conventional dual-loop voltage control.

The plant model from the inverter output voltage v_{i} to the capacitor voltage v_{o} and the inverter-side current i_{i} in the LC system can be derived as

$$T_{\mathrm{vLC}}(s) = \frac{v_{\mathrm{o}}(s)}{v_{\mathrm{i}}(s)} = \frac{1}{s^2 L_{\mathrm{i}} C_{\mathrm{f}} + 1}, \tag{4}$$

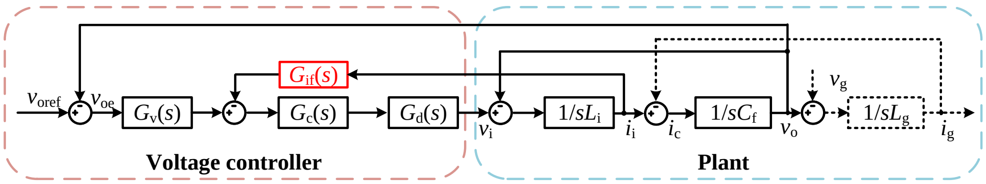

Fig. 2. Voltage control block diagram under stand-alone / LC mode (solid) and grid-tied / LCL mode (solid + dotted).

$$T_{\mathrm{iLC}}(s) = \frac{i_{\mathrm{i}}(s)}{v_{\mathrm{i}}(s)} = \frac{sC_{\mathrm{f}}}{s^2 L_{\mathrm{i}} C_{\mathrm{f}} + 1}. \tag{5}$$

The open loop transfer function of the voltage loop at stand-alone mode is then derived as

$$\begin{aligned} G_{\mathrm{LC}}(s) &= \frac{v_{\mathrm{o}}(s)}{v_{\mathrm{oref}}(s) - v_{\mathrm{o}}(s)} \\ &= \frac{G_{\mathrm{v}}(s) G_{\mathrm{c}}(s) G_{\mathrm{d}}(s) T_{\mathrm{vLC}}(s)}{1 + G_{\mathrm{c}}(s) G_{\mathrm{d}}(s) T_{\mathrm{iLC}}(s)} \\ &= \frac{G_{\mathrm{v}}(s) K_{\mathrm{cp}} G_{\mathrm{d}}(s)}{s^2 L_{\mathrm{i}} C_{\mathrm{f}} + s K_{\mathrm{cp}} G_{\mathrm{d}}(s) C_{\mathrm{f}} + 1} \end{aligned}. \tag{6}$$

When the GFMC is connected to the grid, the plant model of the LCL system is derived as

$$T_{\mathrm{vLCL}}(s) = \frac{v_{\mathrm{o}}(s)}{v_{\mathrm{i}}(s)} = \frac{L_{\mathrm{g}}}{s^2 L_{\mathrm{i}} C_{\mathrm{f}} L_{\mathrm{g}} + L_{\mathrm{i}} + L_{\mathrm{g}}}, \tag{7}$$

$$T_{\mathrm{iLCL}}(s) = \frac{i_{\mathrm{i}}(s)}{v_{\mathrm{i}}(s)} = \frac{s^2 L_{\mathrm{g}} C_{\mathrm{f}} + 1}{s^3 L_{\mathrm{i}} C_{\mathrm{f}} L_{\mathrm{g}} + s(L_{\mathrm{i}} + L_{\mathrm{g}})}, \tag{8}$$

then the open loop transfer function will become

$$\begin{aligned} G_{\mathrm{LCL}}(s) &= \frac{v_{\mathrm{o}}(s)}{v_{\mathrm{oref}}(s) - v_{\mathrm{o}}(s)} \\ &= \frac{G_{\mathrm{v}}(s) G_{\mathrm{c}}(s) G_{\mathrm{d}}(s) T_{\mathrm{vLCL}}(s)}{1 + G_{\mathrm{c}}(s) G_{\mathrm{d}}(s) T_{\mathrm{iLCL}}(s)} \\ &= \frac{G_{\mathrm{v}}(s) K_{\mathrm{cp}} G_{\mathrm{d}}(s) s L_{\mathrm{g}}}{s^3 C_{\mathrm{f}} L_{\mathrm{i}} L_{\mathrm{g}} + K_{\mathrm{cp}} G_{\mathrm{d}}(s) s^2 C_{\mathrm{f}} L_{\mathrm{g}} + s(L_{\mathrm{g}} + L_{\mathrm{i}}) + K_{\mathrm{cp}} G_{\mathrm{d}}(s)} \end{aligned}. \tag{9}$$

Note that the current feedback filter $G_{\mathrm{if}}(s)$ in Fig. 2 is bypassed in (6) and (9).

C. Voltage Loop Dynamics Evaluation

According to (6) and (9), the open loop transfer functions are different under LC and LCL modes. More specifically, the low frequency characteristics have changed a lot because the current models (5) and (8) under the LC and LCL cases are in different formats. Compared to $T_{\mathrm{iLC}}(s)$ in (5), $T_{\mathrm{iLCL}}(s)$ in (8) has one more pole at $s = 0$, which will reduce the type number (TN) of the system $G_{\mathrm{LCL}}(s)$ by 1. The TN refers to the number of poles at the origin of the s plane [27].

The bode diagrams of $G_{\mathrm{LC}}(s)$ and $G_{\mathrm{LCL}}(s)$ are shown in Fig. 3. The system parameters and control parameters are shown in TABLEs I and II, respectively. As observed, $G_{\mathrm{LC}}(s)$ and $G_{\mathrm{LCL}}(s)$ have similar high frequency response. However, during the low frequency range, the slopes of $G_{\mathrm{LC}}(s)$ and $G_{\mathrm{LCL}}(s)$ are $20\,\mathrm{dB\,dec^{-1}}$ and $40\,\mathrm{dB\,dec^{-1}}$, respectively, which results from the TN difference between the two cases. Similarly, because of the TN difference, the initial phase of $G_{\mathrm{LCL}}(s)$ is also $90°$ larger than that of $G_{\mathrm{LC}}(s)$. The high slope of the LCL (grid-tied) open loop transfer function $G_{\mathrm{LCL}}(s)$ at the low frequency range makes the low frequency loop gain poor. Also, the stability margin requirements put limitation on increasing the low frequency loop gain by tuning controller gains. Hence, the voltage tracking speed under the grid-tied mode will be much slower than the stand-alone operation. Note that the controllers and parameters follow the common design guidelines for dual loop voltage controllers for LC/LCL converters to have optimized resonance damping and $3\,\mathrm{dB}$ stability margin [18], [23].

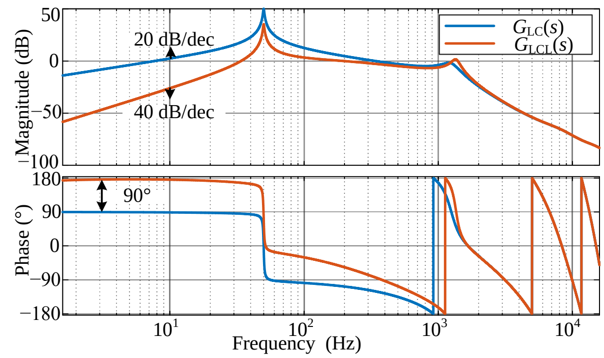

Fig. 3. Bode diagram of $G_{\mathrm{LC}}(s)$ and $G_{\mathrm{LCL}}(s)$ with the conventional dual loop controller.

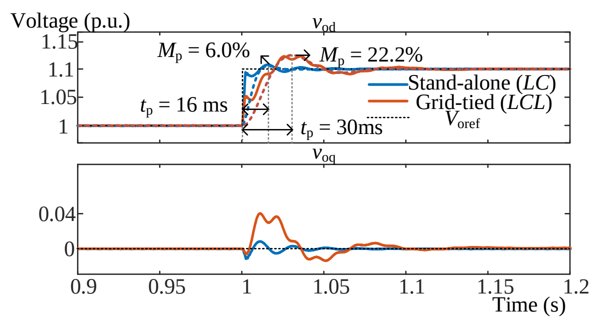

Fig. 4. Voltage step responses (solid) and corresponding 2^{nd} order approximations (dotted) under stand-alone and grid-tied modes.

Fig. 4 shows the simulated waveforms of the voltage step response under the stand-alone and grid-tied modes with same control parameters. As observed, the grid-tied mode response has larger overshoot and settling time than the stand-alone mode, which agrees with the previous analysis. Furthermore, the reduced dynamic response of the voltage control loop is also revealed and analyzed in the synchronous dq frame [28]. This paper is an extension of [28].

D. Approximate Amplitude and Phase Transfer Functions

The voltage controller in a GFMC tracks the voltage amplitude reference V_{oref} and phase reference θ_{oref}, which are dc characteristics of the ac signal. Assuming that the ac voltage amplitude over C_{f} is V_{o}, the phase angle of the GFMC is θ_{o}. The transfer functions from the phase and voltage amplitude references to the relative outputs can be represented as

$$T_{\mathrm{a}}(s) = \frac{\hat{V}_{\mathrm{o}}(s)}{\hat{V}_{\mathrm{oref}}(s)} \approx \frac{\hat{v}_{\mathrm{od}}(s)}{\hat{v}_{\mathrm{odref}}(s)}, \tag{10}$$

$$T_{\mathrm{p}}(s) = \frac{\hat{\theta}_{\mathrm{o}}(s)}{\hat{\theta}_{\mathrm{oref}}(s)} \approx \frac{V_{\mathrm{o}} \sin \hat{\theta}_{\mathrm{o}}(s)}{V_{\mathrm{o}} \sin \hat{\theta}_{\mathrm{oref}}(s)} = \frac{\hat{v}_{\mathrm{oq}}(s)}{\hat{v}_{\mathrm{oqref}}(s)}, \tag{11}$$

TABLE I
SYSTEM PARAMETERS

Description	Symbol	Parameter
Filter inductance	L_{i}	$2\,\mathrm{mH}$
Filter inductance ESR	R_{i}	$0.1\,\Omega$
Filter capacitance	C_{f}	$15\,\mu\mathrm{F}$
Grid inductance	L_{g}	$4\,\mathrm{mH}$
Grid inductance ESR	R_{g}	$0.2\,\Omega$
GFMC power rating	S_{n}	$3000\,\mathrm{VA}$
Nominal ac voltage (peak)	V_{n}	$155\,\mathrm{V}$
Nominal dc voltage	v_{dc}	$400\,\mathrm{V}$
Nominal ac angular frequency	ω_1	$314\,\mathrm{rad\,s^{-1}}$
Sample/switching frequency	$f_{\mathrm{s}}/f_{\mathrm{sw}}$	$10\,\mathrm{kHz}$

TABLE II
CONTROL PARAMETERS

Description	Symbol	Parameter
Active power droop coefficient	D_{p}	$50\,\mathrm{p.u.}$
Rective power droop coefficient	D_{q}	$10\,\mathrm{p.u.}$
Power control cut-off frequency	ω_{f}	$628\,\mathrm{rad\,s^{-1}}$
Voltage control proportional gain	K_{vp}	$0\,\mathrm{S}$
Voltage control resonance gain	K_{vr}	$150\,\mathrm{S\,s^{-1}}$
Current control proportional gain	K_{cp}	$6.7\,\Omega$
R controller damping coefficient	ζ_{r}	0.01
Current feedback filter cutoff frequency	ω_{if}	$2393\,\mathrm{rad\,s^{-1}}$

where the hat ˆ denotes the small perturbation. Because of the symmetry between the d and q axis control, we use the same transfer function $T_{\mathrm{v}}(s)$ to represent $T_{\mathrm{p}}(s)$ and $T_{\mathrm{a}}(s)$. $T_{\mathrm{v}}(s)$ can not be written in a simple form directly based on the system and control parameters even in the synchronous dq frame for the complicated coupling relationships on the LCL components [28]. Alternatively, we approximate $T_{\mathrm{v}}(s)$ with a second order transfer function from the over shoot M_{p} and the peak time t_{p} of the step responses in Fig. 4 [27], i.e.

$$T_{\mathrm{p}}(s) \approx T_{\mathrm{a}}(s) \approx T_{\mathrm{v}}(s) = \frac{{\omega_{\mathrm{v}}}^2}{s^2 + 2\zeta_{\mathrm{v}}\omega_{\mathrm{v}}s + {\omega_{\mathrm{v}}}^2}, \tag{12}$$

where $T_{\mathrm{v}}(s)$ is the second order approximate voltage loop transfer function, $\zeta_{\mathrm{v}} = (1/((\ln M_{\mathrm{p}})/\pi)^2 + 1)^{-1/2}$ represents the damping factor of the second order system, and $\omega_{\mathrm{v}} = \pi(1 - {\zeta_{\mathrm{v}}}^2)^{-1/2}/t_p$ denotes the natural frequency or the phase or amplitude tracking bandwidth [27]. For the LC mode, $\omega_{\mathrm{v}} = 264.5\,\mathrm{rad\,s^{-1}}$, and $\zeta_{\mathrm{v}} = 0.67$. Yet, for the LCL mode, $\omega_{\mathrm{v}} = 114.5\,\mathrm{rad\,s^{-1}}$, and $\zeta_{\mathrm{v}} = 0.40$. To summarize, the voltage control under grid-tied mode is slower and more poorly-damped than that under the stand-alone mode. The dotted line in Fig. 4 shows the approximated second order responses for the stand-alone and grid-tied cases.

III. POWER LOOP MODEL AND VOLTAGE LOOP INFLUENCE

This section will model the power loop of a GFMC firstly, then emphasize the influence of the voltage control dynamics on the overall stability of the power control.

A. Power Loop Modeling

For the system in Fig. 1, assume that the grid phase angle is θ_{g}. The power angle between the GFMC and the grid is

$$\delta = \theta_{\mathrm{o}} - \theta_{\mathrm{g}} = \int (\omega_{\mathrm{o}} - \omega_{\mathrm{g}})dt, \tag{13}$$

where ω_{o} and ω_{g} represents the GFMC and the grid frequency, respectively. Then the active and reactive power flowing from the GFMC to the grid is given by

$$\begin{cases} P = \frac{3V_{\mathrm{o}}[(V_{\mathrm{o}} - V_{\mathrm{g}}\cos\delta_0)R_{\mathrm{g}} + V_{\mathrm{g}}X_{\mathrm{g}}\sin\delta_0]}{2({R_{\mathrm{g}}}^2 + {X_{\mathrm{g}}}^2)} \\ Q = \frac{3V_{\mathrm{o}}[(V_{\mathrm{o}} - V_{\mathrm{g}}\cos\delta_0)X_{\mathrm{g}} - V_{\mathrm{g}}R_{\mathrm{g}}\sin\delta_0]}{2({R_{\mathrm{g}}}^2 + {X_{\mathrm{g}}}^2)} \end{cases}, \tag{14}$$

where δ_0 denotes the steady-state power angle operating point between the GFMC and the grid, $X_{\mathrm{g}} = \omega_1 L_{\mathrm{g}}$ represents the line reactance. Taking partial differential of (14) yields the small signal model of the power control plant, i.e.

$$\begin{cases} \hat{P} = K_{\mathrm{p}\delta}\hat{\delta} + K_{\mathrm{pv}}\hat{V}_{\mathrm{o}} \\ \hat{Q} = K_{\mathrm{q}\delta}\hat{\delta} + K_{\mathrm{qv}}\hat{V}_{\mathrm{o}} \end{cases}, \tag{15}$$

where the coefficients $K_{\mathrm{p}\delta}$, K_{pv}, $K_{\mathrm{q}\delta}$ and K_{qv} are expressed as

$$\begin{cases} K_{\mathrm{p}\delta} = \frac{3V_{\mathrm{o}}V_{\mathrm{g}}(R_{\mathrm{g}}\sin\delta_0 + X_{\mathrm{g}}\cos\delta_0)}{2(R_{\mathrm{g}}^2 + X_{\mathrm{g}}^2)} \\ K_{\mathrm{pv}} = \frac{3(2V_{\mathrm{o}}R_{\mathrm{g}} + V_{\mathrm{g}}(-R_{\mathrm{g}}\cos\delta_0 + X_{\mathrm{g}}\sin\delta_0))}{2(R_{\mathrm{g}}^2 + X_{\mathrm{g}}^2)} \\ K_{\mathrm{q}\delta} = \frac{3V_{\mathrm{o}}V_{\mathrm{g}}(-R_{\mathrm{g}}\cos\delta_0 + X_{\mathrm{g}}\sin\delta_0)}{2(R_{\mathrm{g}}^2 + X_{\mathrm{g}}^2)} \\ K_{\mathrm{qv}} = \frac{3(2V_{\mathrm{o}}X_{\mathrm{g}} + V_{\mathrm{g}}(-R_{\mathrm{g}}\sin\delta_0 - X_{\mathrm{g}}\cos\delta_0))}{2(R_{\mathrm{g}}^2 + X_{\mathrm{g}}^2)} \end{cases}. \tag{16}$$

Noted that for an inductive transmission line where $X_{\mathrm{g}} \gg R_{\mathrm{g}}$, K_{pv} and $K_{\mathrm{q}\delta}$ are much smaller than $K_{\mathrm{p}\delta}$ and K_{qv}.

The power controllers feed back P and Q through a low pass filter (LPF) $G_{\mathrm{f}}(s) = \omega_{\mathrm{f}}/(s + \omega_{\mathrm{f}})$, which can be written in the form of

$$\begin{cases} P_{\mathrm{mpu}}(s) = G_{\mathrm{f}}(s)P(s)/S_{\mathrm{n}} \\ Q_{\mathrm{mpu}}(s) = G_{\mathrm{f}}(s)Q(s)/S_{\mathrm{n}} \end{cases}, \tag{17}$$

where ω_{f} is the cutoff frequency, S_{n} is the rated capacity of the GFMC, P_{mpu} and Q_{mpu} are the per unit value of the measured P and Q, respectively. In the active power controller (APC), the frequency reference ω_{oref} of the GFMC is designed as

$$\omega_{\mathrm{oref}} = (P_{\mathrm{ref}} - P_{\mathrm{mpu}})\omega_1/D_{\mathrm{p}} + \omega_1, \tag{18}$$

where D_{p} represents the active power droop gain in per unit form. Similarly, droop control is also used in the reactive power controller (RPC). The voltage reference V_{oref} for the GFMC is chosen as

$$V_{\mathrm{oref}} = (Q_{\mathrm{ref}} - Q_{\mathrm{mpu}})V_{\mathrm{n}}/D_{\mathrm{q}} + V_{\mathrm{n}} \tag{19}$$

where V_{n} is the nominal voltage, D_{q} stands for the per unit reactive power droop gain. The active and reactive power controller $G_{\mathrm{p}}(s)$ and $G_{\mathrm{q}}(s)$ can be written in the form of

$$\begin{cases} G_{\mathrm{p}}(s) = \frac{\theta_{\mathrm{oref}}(s)}{P_{\mathrm{ref}}(s) - P_{\mathrm{mpu}}(s)} = \frac{\omega_1}{D_{\mathrm{p}}s} \\ G_{\mathrm{q}}(s) = \frac{V_{\mathrm{oref}}(s)}{Q_{\mathrm{ref}}(s) - Q_{\mathrm{mpu}}(s)} = \frac{V_{\mathrm{n}}}{D_{\mathrm{q}}} \end{cases}. \tag{20}$$

Combining the small signal model of the plant and the controllers will finally yield the power loop control block diagram illustrated in Fig. 5, where $\hat{P}_{\mathrm{f}}$ and $\hat{Q}_{\mathrm{f}}$ represent the per unit filtered active and reactive power, respectively. The active power open loop transfer function $G_{\mathrm{p\_open}}(s)$ is defined as the product of the forward and feedback path transfer functions between $\hat{P}_{\mathrm{ref}}$ and $\hat{P}$ in Fig. 5, which can be derived as

$$\begin{aligned} G_{\mathrm{p\_open}}(s) &= \frac{\hat{P}_{\mathrm{f}}(s)}{\hat{P}_{\mathrm{ref}}(s) - \hat{P}_{\mathrm{f}}(s)} \\ &= \frac{G_{\mathrm{p}}(s)T_{\mathrm{v}}(s)G_{\mathrm{f}}(s)}{S_{\mathrm{n}}} \cdot (K_{\mathrm{p}\delta} + \frac{K_{\mathrm{q}\delta}K_{\mathrm{pv}}G_{\mathrm{q}}(s)T_{\mathrm{v}}(s)G_{\mathrm{f}}(s)/S_{\mathrm{n}}}{1 + K_{\mathrm{qv}}G_{\mathrm{q}}(s)T_{\mathrm{v}}(s)G_{\mathrm{f}}(s)/S_{\mathrm{n}}}) \end{aligned}. \tag{21}$$

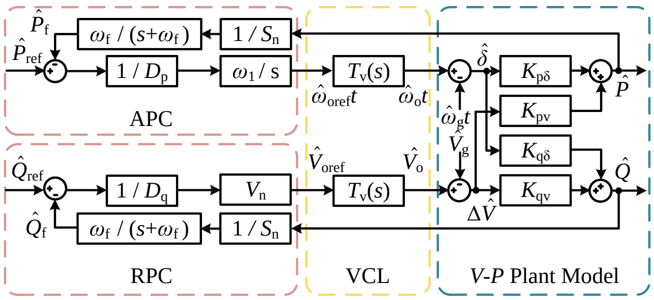

Fig. 5. Power control model.

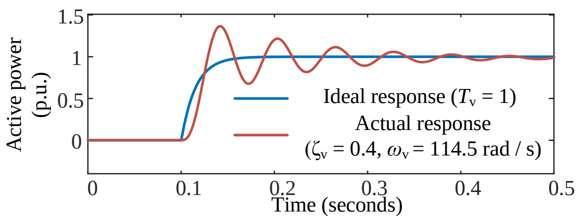

Fig. 6. Step responses of active power.

In (21), K_{pv} and $K_{\mathrm{q}\delta}$ are very small compared to $K_{\mathrm{p}\delta}$, so $G_{\mathrm{p\_open}}(s)$ can be further approximated as

$$G_{\mathrm{p\_open}}(s) \approx G_{\mathrm{p}}(s)T_{\mathrm{v}}(s)G_{\mathrm{f}}(s)K_{\mathrm{p}\delta}/S_{\mathrm{n}} \tag{22}$$

From (22), the power loop bandwidth is inversely proportional to the droop coefficient D_{p}, the converter capacity S_{n} and the grid impedance X_{g}, where D_{p} associates with $G_{\mathrm{p}}(s)$ in (20) and X_{g} relates to the coefficients $K_{\mathrm{p}\delta}$. Specifically, GFMCs with small capacities or droop coefficients, or connected to the grid through small impedance will have fast power loops. The power loop bandwidth may vary from $0.1\,\mathrm{Hz}$ to $10\,\mathrm{Hz}$ [7], [29].

B. Interaction between Power Loop and Voltage Loop

Fig. 6 plots the active power step response of the ideal active power loop with $T_{\mathrm{v}}(s) = 1$ and the actual power loop response when $T_{\mathrm{v}}(s)$ is represented with (12). With the open loop transfer function in (21) and the parameters in TABLEs I and II, the ideal active power loop bandwidth can be calculated as $8.8\,\mathrm{Hz}$ with a phase margin of $85°$. As illustrated in Fig. 6, the designed power loop response is fast and smooth. Nonetheless, the actual active power response oscillates and takes more time to settle. As analyzed in Section II-D, when the GFMC is connected to the grid, the damping ratio drops to $\zeta_{\mathrm{v}} = 0.40$, and the voltage control bandwidth decreases to $\omega_{\mathrm{v}} = 114.5\,\mathrm{rad\,s^{-1}}$, i.e. $18.2\,\mathrm{Hz}$. Because the voltage loop is poorly damped, and its bandwidth is close to the power loop bandwidth, the power loop response gets undesirable. To reduce the interaction between the power loop and the voltage loop, we design a voltage controller with improved dynamics.

IV. Dynamic Enhanced Voltage Controller

This section will propose a generic control scheme to improve the voltage reference tracking performance. Then the overall control parameter design guideline will be given.

A. Control Architecture Design

It can be concluded from the previous analysis based on (6) and (9) that the reduced dynamic response of the GFMC under the grid-tied mode mainly results from the TN changing, i.e. the zero of $G_{\mathrm{LCL}}(s)$ at the origin introduced by the current feedback loop when the grid impedance is considered. In order to achieve similar satisfied dynamics under both stand-alone and grid-tied modes, we need to cancel the pole of $T_{\mathrm{iLCL}}(s)$ at $s = 0$, i.e. add a zero in the current feedback loop in the low frequency range. Moreover, the resonance damping function in the high frequency range should be kept simultaneously. As a solution, we add a high-pass filter (HPF) $G_{\mathrm{if}}(s)$ to the current feedback path as shown in Fig. 1 and Fig. 2. The HPF is implemented in the stationary frame, which is expressed as

$$G_{\mathrm{if}}(s) = s/(s+\omega_{\mathrm{if}}), \tag{23}$$

where ω_{if} is the cutoff frequency of the HPF. After employing the HPF, the voltage control open loop transfer function under LC and LCL modes will become

$$\begin{aligned} G_{\mathrm{LC}}(s) &= \frac{v_{\mathrm{o}}(s)}{v_{\mathrm{oref}}(s)-v_{\mathrm{o}}(s)} \\ &= \frac{G_{\mathrm{v}}(s)G_{\mathrm{c}}(s)G_{\mathrm{d}}(s)T_{\mathrm{vLC}}(s)}{1+G_{\mathrm{c}}(s)G_{\mathrm{d}}(s)G_{\mathrm{if}}(s)T_{\mathrm{iLC}}(s)} \\ &= \frac{G_{\mathrm{v}}(s)K_{\mathrm{cp}}G_{\mathrm{d}}(s)}{s^2L_{\mathrm{i}}C_{\mathrm{f}}+s^2G_{\mathrm{d}}(s)K_{\mathrm{cp}}C_{\mathrm{f}}/(s+\omega_{\mathrm{if}})+1} \end{aligned}, \tag{24}$$

$$\begin{aligned} G_{\mathrm{LCL}}(s) &= \frac{v_{\mathrm{o}}(s)}{v_{\mathrm{oref}}(s)-v_{\mathrm{o}}(s)} \\ &= \frac{G_{\mathrm{v}}(s)G_{\mathrm{c}}(s)G_{\mathrm{d}}(s)T_{\mathrm{vLCL}}(s)}{1+G_{\mathrm{c}}(s)G_{\mathrm{d}}(s)G_{\mathrm{if}}(s)T_{\mathrm{iLCL}}(s)} \\ &= \frac{G_{\mathrm{v}}(s)K_{\mathrm{cp}}G_{\mathrm{d}}(s)L_{\mathrm{g}}}{s^2C_{\mathrm{f}}L_{\mathrm{i}}L_{\mathrm{g}}+\frac{K_{\mathrm{cp}}G_{\mathrm{d}}(s)s^2C_{\mathrm{f}}L_{\mathrm{g}}}{(s+\omega_{\mathrm{if}})}+(L_{\mathrm{g}}+L_{\mathrm{i}})+\frac{K_{\mathrm{cp}}G_{\mathrm{d}}(s)}{(s+\omega_{\mathrm{if}})}} \end{aligned}. \tag{25}$$

As observed in (25), the zero at $s = 0$ in (9) introduced by the current loop is canceled by introducing the HPF $G_{\mathrm{if}}(s)$. As a result, the TN of $G_{\mathrm{LC}}(s)$ and $G_{\mathrm{LCL}}(s)$ becomes the same after employing the HPF in the current feedback path.

The bode diagram of the voltage control open loop gain with the filtered current feedback under stand-alone (LC) and grid-tied (LCL) mode is shown in Fig. 7. As observed, the HPF mitigates the current loop influence on the low frequency range while retaining the resonance frequency damping effect at the higher frequency range. The loop gain under the grid-tied (LCL) case is improved significantly especially in the low frequency range when compared to the conventional dual loop voltage controlled GFMC under the grid-tied (LCL) case. At the same time, the open loop gain under the stand-alone (LC) case and the high frequency part of the grid-tied (LCL) case have no serious difference after adding the HPF.

Fig. 8 shows the comparison of the voltage reference tracking dynamics simulation under the grid-tied operation with and without applying the proposed HPF in the current feedback loop. Except for the HPF $G_{\mathrm{if}}(s)$, the control structures and parameters are the same. As observed, after applying the HPF, the settling time t_{s} corresponding to a $\pm\ 5\,\%$ error band is reduced from $71\,\mathrm{ms}$ to $17\,\mathrm{ms}$, and the overshoot M_{p} is also reduced from $22.2\,\%$ to $5.6\,\%$, showing a great improvement in the voltage reference tracking performance with faster speed and less oscillations.

Note that although the HPF in the feedback path will make it harder to add current saturation directly in the cascaded

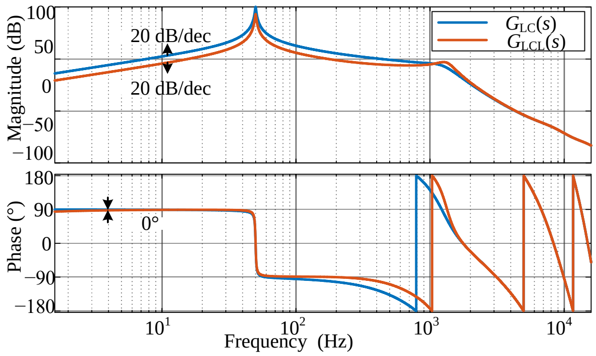

Fig. 7. Bode diagram of $G_{\mathrm{LC}}(s)$ and $G_{\mathrm{LCL}}(s)$ with filtered current feedback damping.

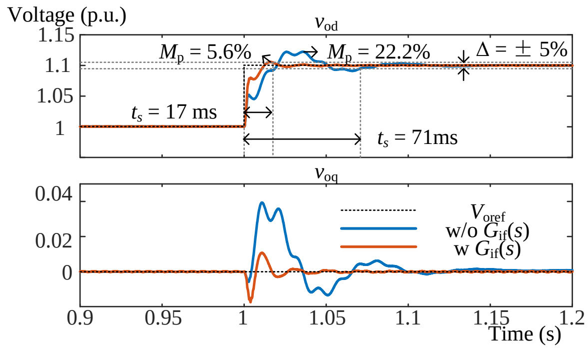

Fig. 8. Voltage step responses without and with the current feedback filter $G_{\mathrm{if}}(s)$ under the grid-tied operation.

control path, yet the current information can still be used to limit the current. [30] proposed a current limiting method that can be applied to any forms of voltage controllers even without a current loop. Hence, the proposed HPF in the feedback path will not impede current limiting in GFMCs.

B. Control Parameter Design

The design of LCL parameters in dual loop voltage control schemes basically follows the rule of not introducing negative virtual resistances to the system, i.e. $f_{\mathrm{r}} < f_{\mathrm{s}}/6$ [18], [23].

The main control parameters to be designed are the voltage controller gains K_{vp} and K_{vr}, the current controller gain K_{cp}, and the filter cutoff frequency ω_{if}.

Firstly, K_{cp}, K_{vp} and K_{vr} are designed based on the dual loop voltage control structure without considering $G_{\mathrm{if}}(s)$. As mentioned before, the function of the current loop is to damp the LC/LCL resonance. Because of the computation and PWM delay, there is a boundary value and an optimized value for K_{cp} [18]. K_{cp} should be smaller than the boundary value to achieve positive damping. At the optimized K_{cp}, the damping performance is the best. The boundary and optimized K_{cp} values for LC and LCL cases are different. In this paper, K_{cp} is chosen as $6.7\,\Omega$ to achieve a satisfied damping effect under both LC and LCL cases [18].

The R controller is chosen because it has a wider control bandwidth than the PR controller in the dual loop voltage control under the same stability requirements [23]. As a result, K_{vp} is assigned with $0\,\mathrm{S}$, and K_{vi} is selected as $150\,\mathrm{S\,s^{-1}}$ to achieve a $3\,\mathrm{dB}$ gain margin.

Then the HPF cutoff frequency ω_{if} is designed. To ensure enough resonance damping at the resonance peak, we require the current loop gain has at least 0.9 of the original loop gain at the LC resonance frequency, which yields

$$|G_{\mathrm{if}}(j\omega_{\mathrm{rLC}})| = \omega_{\mathrm{rLC}}/\sqrt{{\omega_{\mathrm{rLC}}}^2 + {\omega_{\mathrm{if}}}^2} \geq 0.9, \tag{26}$$

where $\omega_{\mathrm{rLC}} = 1/\sqrt{L_{\mathrm{i}}C_{\mathrm{f}}}$ is the LC resonance frequency. Based on the system parameters given in TABLE I, ω_{cf} is assigned with $2393\,\mathrm{rad\,s^{-1}}$.

C. Physical Explanation of HPF in Current Feedback Path

As revealed in Section II, the deteriorated dynamic response of GFMCs under the grid-tied mode is caused by the inverter-side current model changing when connected to the grid, which worsens the low-frequency response. On the contrary, the model of the capacitor current i_c will not change its form under both grid-tied and stand-alone modes, whose models under the stand-alone and grid-tied modes are expressed as

$$T_{\mathrm{icLC}}(s) = \frac{i_{\mathrm{c}}(s)}{v_{\mathrm{i}}(s)} = \frac{sC_{\mathrm{f}}}{s^2 L_{\mathrm{i}} C_{\mathrm{f}} + 1}, \tag{27}$$

$$T_{\mathrm{icLCL}}(s) = \frac{i_{\mathrm{c}}(s)}{v_{\mathrm{i}}(s)} = \frac{sL_{\mathrm{g}}C_{\mathrm{f}}}{s^2 L_{\mathrm{i}} C_{\mathrm{f}} L_{\mathrm{g}} + (L_{\mathrm{i}} + L_{\mathrm{g}})}, \tag{28}$$

respectively. As a result, using the capacitor current feedback damping [17] will not worsen the dynamic response of the voltage control under the grid-tied mode. The LCL filter smooths the output current i_{g}, which means the high-frequency signals in the inverter-side current i_{i} go to the capacitor. Consequently, using a HPF in the inverter-side current can be interpreted as emulating the capacitor current feedback active damping. Compared to using the capacitor current as the inner loop, using a HPF in the converter output current can improve the voltage control dynamics without introducing extra current sensors.

D. Controller Discretization

Although the system modeling and the controller design are conducted in the continuous-time domain, the implementation of the controllers is conducted in the discrete-time domain. The controllers in the s domain are mapped to the z domain using the Tustin's method, i.e. the substitution of

$$s \leftarrow \frac{2}{T_s}\frac{z-1}{z+1}. \tag{29}$$

Since the voltage control bandwidth is much lower than the switching frequency, the approximate continuous-time analysis conclusions can be applied to the actual discrete-time system.

V. Discussion

This section first reveals the similar dynamic response worsening problem in different voltage control schemes, then reviews other commonly used state feedback control methods for LC/LCL filtered power converters. The conclusion is that some of these methods are equivalent and may also be applied to solve the problem discovered in this paper.

A. Dynamic Response Reduction Problem in Other Control Schemes

The reduced dynamic response not only exists in the dual loop voltage control scheme discussed in Section II, but also exists in other control schemes whenever the inverter-side current is utilized for resonance damping, even when high-bandwidth controllers are designed under stand-alone cases. With the same dual loop control structure in Fig. 2, the voltage controller $G_{\mathrm{v}}(s)$ can take other forms, such as proportional resonance with integral (PR-I) controller and integral plus resonance (IR) controllers [23]. These I-based controllers have a wider bandwidth than the R or PR controllers used in this paper, while the similar TN changing and reduced dynamic response also exists because of the same control structures. Another widely used control structure is the dual loop voltage control with voltage feedback decoupling. This control structure has extremely fast response under the stand-alone mode, while the TN will decrease by two when the GFMC is connected to the grid, which will also lead to the reduced dynamic response. The proposed filtered current feedback method can also improve the voltage tracking dynamics in the above-mentioned control structures.

B. Review of State Feedback Control for LC/LCL Filtered Power Converters

This paper proposed a filtered current feedback voltage control strategy to improve the voltage control dynamics for grid-forming converters under the grid-tied operation. In addition to the proposed method, there are many other state feedback control with filtering methods to improve the system performances. Here we summarized these control methods as shown in TABLE III. Besides the summarized methods for special functions, [31] also gives a thorough review of virtual impedance implementation with different control variables and filter combinations for aims of damping, disturbance rejection and auxiliary services. Most of the summarized methods study the stability problems of the grid-feeding converters, and aiming at improving the LC/LCL resonance damping, widening the stable region of the resonance frequency, and mitigating the computation delay. This paper fills the gap of improving the low-frequency response of the dual-loop voltage controller under the grid-tied mode. Note that the poor dynamic response of GFMCs under the grid-tied mode can be improved through various state feedback control methods, such as capacitor current feedback method mentioned in section IV-C and emulating the capacitor current by taking the derivative of capacitor voltage as shown in Table III. The grid-side virtual impedance can also relieve this problem to some extent, but the voltage deviation caused by the grid-side virtual impedance will put stress on the voltage quality and the power regulation. Despite various solutions, the contributions of this paper focus more on revealing the poor voltage tracking dynamic problem when implementing the dual-loop voltage control with the inverter-side current as the inner loop and providing a possible solution.

VI. Experimental Results

We compared the performance of the conventional dual-loop voltage controller and the proposed filtered current feedback voltage controller under the cases of stand-alone/grid-tied modes and with/without power control loop modes based on the schematic diagram shown in Fig. 1. The system and control parameters are listed in TABLE I and II. The experimental results verify that the proposed controller can improve the voltage tracking dynamics and the power control stability when the grid-forming converter is connected to the grid. An off-grid RL load step increase test indicates that the proposed controller will not influence the normal operation under the stand-alone mode.

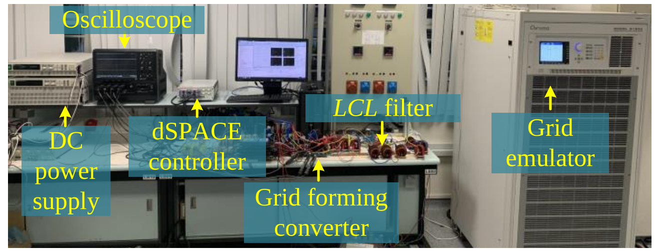

Fig. 9. Experimental Setup.

Fig. 9 shows the photo of the experimental setup. The grid-emulator Chroma 61830 was connected to the grid-forming converter through grid inductors. The grid-forming converter was fed by a constant voltage dc power supply and controlled by dSPACE (microlabbox) control platform. An 8-channel oscilloscope was employed to capture the experimental waveforms. The experimental results are shown in Fig. 10–14.

A. Voltage Reference Tracking Test

To illustrate the difference of the voltage reference tracking dynamics when the GFMC is under stand-alone and grid-tied modes, and to show improvements in voltage tracking with the proposed controller under the grid-tied mode, voltage reference step experiments were conducted. As known, severe voltage differences between two voltage sources will cause

TABLE III
Control Variables and Filters Combinations

Feedback item	Filter type	Target	Ref
Capacitor voltage	Proportional gain	Active damping	[20]
	Low-pass	Widen stable region	[22], [32]
	Digital derivative	Emulate capacitor current	[33], [34]
	Lead compensator	Mitigate computation delay	[32], [35]
	High-pass	Virtual harmonic damper	[36]
Capacitor current	Proportional gain	Active damping	[37]
PCC voltage	Proportional gain	Widen stable region	[19], [38]
Grid current	Negative HPF	Mitigate computation delay	[39]
Inverter current	Proportional gain	Active damping	[18]
	Notch filter (Utility frequency)	Emulate grid current	[16]
	Notch filter (LCL resonance frequency)	Cancel LCL resonance	[33]

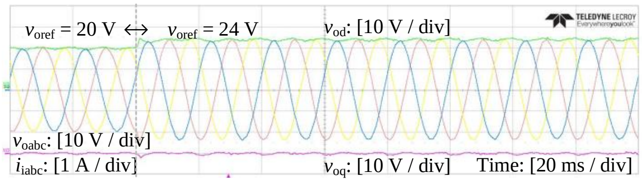

(a)

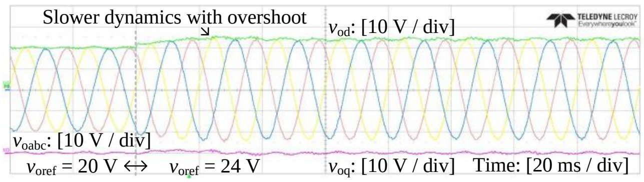

(b)

Fig. 10. Experimental waveforms of the conventional dual loop voltage controller under a $20\,\%$ voltage step change. (a). Stand-alone mode. (b). Grid-tied mode.

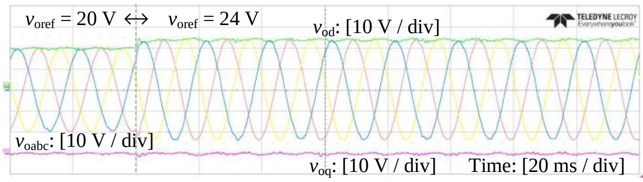

(a)

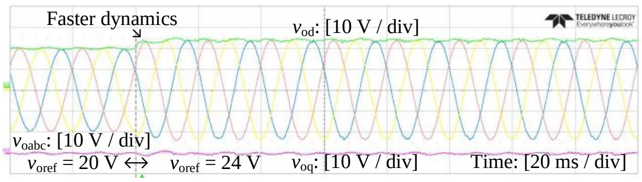

(b)

Fig. 11. Experimental waveforms of the dual loop voltage controller with high-pass filtered current feedback under a $20\,\%$ voltage step change. (a). Stand-alone mode. (b). Grid-tied mode.

large short-circuit current. In order to show the voltage tracking dynamics changing clearly without causing over-current, in voltage reference step experiments, the peak voltage was set at $20\,\mathrm{V}$. The GFMC and the grid emulator were intentionally designed to have the same frequency and phase angle.

Fig. 10 illustrates the voltage waveforms when the conventional dual loop voltage controlled GFMC undergoing a $20\,\%$ $(4\,\mathrm{V})$ voltage reference step change. As observed, in Fig. 10(a), when the GFMC was disconnected from the grid, the voltage v_{oabc} tracked the voltage reference quickly and arrived at a steady state in less than $10\,\mathrm{ms}$. However, in Fig. 10(b), when the GFMC with the conventional dual loop voltage controller was connected to the grid, the transient of the voltage reference tracking became oscillatory and slow. An overshoot existed and the voltage arrived at the steady state in longer than $50\,\mathrm{ms}$, which was much slower than the stand-alone case and conformed to the analysis in Section III.

Fig. 11 shows the voltage waveforms when the GFMC with the proposed controller undergoes a $20\,\%$ $(4\,\mathrm{V})$ voltage reference step change. The stand-alone voltage tracking performance presented in Fig. 11(a) was as fast as that with the conventional dual-loop controller in Fig. 10(a). Contrary to Fig. 10(b), when connected to the grid, the GFMC with the proposed controller tracked the reference much faster and arrived at the steady state within $10\,\mathrm{ms}$ as shown in Fig. 11(b), validating the effectiveness of the proposed controller. The experimental waveforms of the grid-tied operation without and with the proposed controller conformed to the simulation results as shown in Fig. 8.

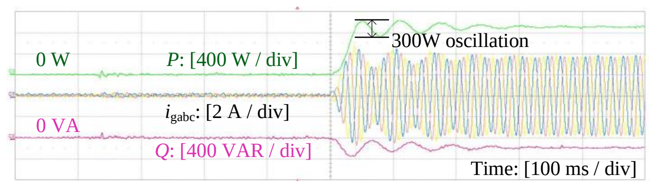

Fig. 12. Experimental waveforms of the conventional dual-loop voltage controller under a $900\,\mathrm{W}$ $(30\,\%)$ power reference step change.

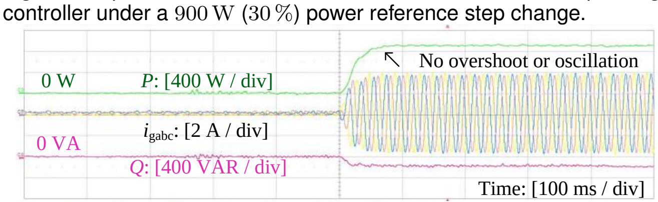

Fig. 13. Experimental waveforms of the dual-loop voltage controller with high-pass filtered current feedback under a $900\,\mathrm{W}$ $(30\,\%)$ power reference step change.

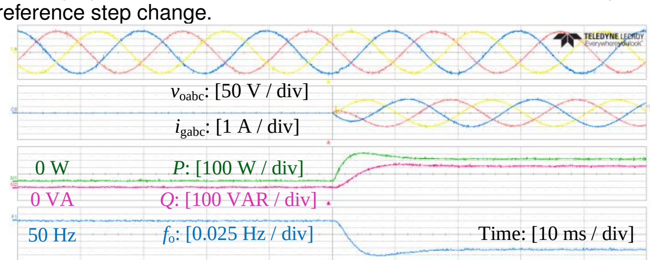

Fig. 14. Experimental waveforms of the dual-loop voltage controller with high-pass filtered current feedback under a step increase of RL load with stand-alone operation.

B. Tests Including the Power Loop

Fig. 12 and Fig. 13 tests the controller performances under the close-loop power control condition. The nominal peak voltage and nominal power were selected as $155\,\mathrm{V}$ and $3000\,\mathrm{W}$ for this set of experiments. The ideal response of the power control loop was a first order response with the bandwidth of $8.8\,\mathrm{Hz}$. In the experiments, the active power reference for the GFMC stepped from $0\,\mathrm{W}$ to $900\,\mathrm{W}$. In Fig. 12, the conventional dual-loop voltage controller was employed. As noticed, when the active power reference changed, a strong oscillation existed in the output power and currents waveforms. The peak-to-peak value of the oscillation reached up to $300\,\mathrm{W}$, which was $33.3\,\%$ of the step reference value. Also, it took longer time than expected from the designed power loop (settling time of $72\,\mathrm{ms}$) to converge to a steady state. In contrast, in Fig. 13, when the proposed controller was applied, the power waveforms responded to the active power reference change quickly without any overshoot. As observed, the power response corresponded with the designed power loop characteristic with the designed faster voltage controller.

When the power references change, there was a small amount of reactive power change in both Fig. 12 and Fig. 13. The reactive power deviation was caused by the cross-coupling between the active and reactive power as shown in Fig. 5. As the reactive power control used droop control instead of the non-steady-state-error control in this work, the reactive power would not converge to 0 VAR, while the droop control would tend to reduce the reactive power deviation by tuning the voltage amplitude reference.

Fig. 14 shows the stand-alone operation of the GFMC with the proposed controller under an RL load step change. The active and reactive power references were set at $P_{\rm ref} = 0\,\mathrm{W}$ and $Q_{\rm ref} = 0\,\mathrm{VAR}$, respectively. The RL load value was chosen as $R_{\rm L} = 54\,\Omega$, $L_{\rm L} = 171\,\mathrm{mH}$. The waveforms of the output voltage $v_{\rm oabc}$, load current $i_{\rm gabc}$, active and reactive power P and Q, and the output frequency $f_{\rm o}$ are shown in Fig. 14. When the RL load was suddenly connected to the converter, the current increased smoothly and the voltage was well regulated. The active and reactive power outputs were around $320\,\mathrm{W}$ and $310\,\mathrm{VAR}$, respectively. As the droop control was applied and the output power was different from the setting value of $0\,\mathrm{W}$, the frequency deviated from its nominal value around $-0.106\,\mathrm{Hz}$. The RL load step experiment shows that the GFMC with the proposed controller can work well under the stand-alone operation.

VII. Conclusion

A well-designed fast voltage loop is important for the control loop decoupling and stable operation of LC/LCL-filtered GFMCs especially when the power loop bandwidth is high. This paper reveals with detailed analysis that the conventional dual-loop voltage control with the inverter-side current feedback as the resonance damping has poorer dynamics when connected to the grid than operating in the stand-alone mode, which may threaten the stability of the power control loop. To improve the voltage tracking dynamics and the power control stability of GFMCs under the grid-tied mode, the dual-loop control is enhanced by applying a HPF in the current feedback path. GFMCs with the proposed generic voltage controller have fast and stable responses under both stand-alone and grid-tied modes. The correctness of the analysis and the effectiveness of the proposed controller is verified by the experiments.

References

[1] D. E. Olivares, A. Mehrizi-Sani, A. H. Etemadi, C. A. Canizares, R. Iravani, M. Kazerani, A. H. Hajimiragha, O. Gomis-Bellmunt, M. Saeedifard, R. Palma-Behnke, G. A. Jimenez-Estevez, and N. D. Hatziargyriou, "Trends in microgrid control," *IEEE Trans. Smart Grid*, vol. 5, no. 4, pp. 1905–1919, 2014.

[2] J. Rocabert, A. Luna, F. Blaabjerg, and P. RodrÃguez, "Control of power converters in ac microgrids," *IEEE Trans. Power Electron.*, vol. 27, no. 11, pp. 4734–4749, 2012.

[3] M. Ashabani and Y. A.-R. I. Mohamed, "Integrating vscs to weak grids by nonlinear power damping controller with self-synchronization capability," *IEEE Trans. Power Syst.*, vol. 29, no. 2, pp. 805–814, 2014.

[4] R. H. Lasseter, Z. Chen, and D. Pattabiraman, "Grid-forming inverters: A critical asset for the power grid," *IEEE J. Emerging Sel. Top. Power Electron.*, vol. 8, no. 2, pp. 925–935, 2020.

[5] J. M. Guerrero, J. C. Vasquez, J. Matas, M. Castilla, and L. G. de Vicuna, "Control strategy for flexible microgrid based on parallel line-interactive ups systems," *IEEE Trans. Ind. Electron.*, vol. 56, no. 3, pp. 726–736, 2009.

[6] L. Zhang, L. Harnefors, and H.-P. Nee, "Interconnection of two very weak ac systems by vsc-hvdc links using power-synchronization control," *IEEE Trans. Power Syst.*, vol. 26, no. 1, pp. 344–355, 2011.

[7] Z. Qing-Chang, N. Phi-Long, M. Zhenyu, and S. Wanxing, "Self-synchronized synchronverters: Inverters without a dedicated synchronization unit," *IEEE Trans. Power Electron.*, vol. 29, no. 2, pp. 617–630, 2014.

[8] S. D'Arco and J. A. Suul, "Equivalence of virtual synchronous machines and frequency-droops for converter-based microgrids," *IEEE Trans. Smart Grid*, vol. 5, no. 1, pp. 394–395, 2014.

[9] J. Liu, Y. Miura, and T. Ise, "Comparison of dynamic characteristics between virtual synchronous generator and droop control in inverter-based distributed generators," *IEEE Trans. Power Electron.*, vol. 31, no. 5, pp. 3600–3611, 2016.

[10] H. Wu, X. Ruan, D. Yang, X. Chen, W. Zhao, Z. Lv, and Q.-C. Zhong, "Small-signal modeling and parameters design for virtual synchronous generators," *IEEE Trans. Ind. Electron.*, vol. 63, no. 7, pp. 4292–4303, 2016.

[11] Y. Qi, H. Deng, X. Liu, and Y. Tang, "Synthetic inertia control of grid-connected inverter considering the synchronization dynamics," *IEEE Transactions on Power Electronics*, vol. 37, no. 2, pp. 1411–1421, 2022.

[12] J. Fang, H. Deng, N. Tashakor, F. Blaabjerg, and S. M. Goetz, "State-space modeling and control of grid-tied power converters with capacitive/battery energy storage and grid-supportive services," *IEEE Journal of Emerging and Selected Topics in Power Electronics*, pp. 1–1, 2021.

[13] Y. Qi, H. Deng, J. Wang, and Y. Tang, "Passivity-based synchronization stability analysis for power-electronic-interfaced distributed generations," *IEEE Trans. on Sustainable Energy*, pp. 1–1, 2020.

[14] K. Guo, Y. Qi, J. Yu, D. Frey, and Y. Tang, "A converter based power system stabilizer for stability enhancement of droop controlled islanded microgrids," *IEEE Trans. Smart Grid*, pp. 1–1, 2021.

[15] P. C. Loh and D. G. Holmes, "Analysis of multiloop control strategies for lc/cl/lcl-filtered voltage-source and current-source inverters," *IEEE Trans. Ind. Appl.*, vol. 41, no. 2, pp. 644–654, 2005.

[16] Y. Tang, P. C. Loh, P. Wang, F. H. Choo, and F. Gao, "Exploring inherent damping characteristic of lcl-filters for three-phase grid-connected voltage source inverters," *IEEE Trans. Power Electron.*, vol. 27, no. 3, pp. 1433–1443, 2012.

[17] D. Pan, X. Ruan, C. Bao, W. Li, and X. Wang, "Capacitor-current-feedback active damping with reduced computation delay for improving robustness of lcl-type grid-connected inverter," *IEEE Trans. Power Electron.*, vol. 29, no. 7, pp. 3414–3427, 2014.

[18] Y. Geng, Y. Yun, R. Chen, K. Wang, H. Bai, and X. Wu, "Parameters design and optimization for lc-type off-grid inverters with inductor-current feedback active damping," *IEEE Trans. Power Electron.*, vol. 33, no. 1, pp. 703–715, 2018.

[19] J. M. Gonzalez, C. A. Busada, and J. A. Solsona, "A robust controller for a grid-tied inverter connected through an lcl filter," *IEEE Journal of Emerging and Selected Topics in Industrial Electronics*, vol. 2, no. 1, pp. 82–89, 2021.

[20] H. Zhang, X. Ruan, Z. Lin, L. Wu, Y. Ding, and Y. Guo, "Capacitor voltage full feedback scheme for lcl-type grid-connected inverter to suppress current distortion due to grid voltage harmonics," *IEEE Trans. Power Electron.*, vol. 36, no. 3, pp. 2996–3006, 2021.

[21] Y. Geng, X. Song, X. Zhang, K. Yang, and H. Liu, "Stability analysis and key parameters design for grid-connected current-source inverter with capacitor-voltage feedback active damping," *IEEE Trans. Power Electron.*, vol. 36, no. 6, pp. 7097–7111, 2021.

[22] X. Wang, P. C. Loh, and F. Blaabjerg, "Stability analysis and controller synthesis for single-loop voltage-controlled vsis," *IEEE Trans. Power Electron.*, vol. 32, no. 9, pp. 7394–7404, 2017.

[23] Y. Liao, X. Wang, and F. Blaabjerg, "Passivity-based analysis and design of linear voltage controllers for voltage-source converters," *IEEE Open J. Ind. Electron. Soc.*, vol. 1, pp. 114–126, 2020.

[24] S. D. Arco, J. A. Suul, and O. B. Fosso, "Small-signal modelling and parametric sensitivity of a virtual synchronous machine," in *2014 Power Systems Computation Conference*, 2014, Conference Proceedings, pp. 1–9.

[25] J. Fang, H. Li, Y. Tang, and F. Blaabjerg, "On the inertia of future more-electronics power systems," *IEEE Journal of Emerging and Selected Topics in Power Electronics*, vol. 7, no. 4, pp. 2130–2146, 2019.

[26] C. Zou, B. Liu, S. Duan, and R. Li, "Stationary frame equivalent model of proportional-integral controller in dq synchronous frame," *IEEE Trans. Power Electron.*, vol. 29, no. 9, pp. 4461–4465, 2014.

[27] G. F. Franklin, D. J. Powell, and A. Emami-Naeini, *Feedback Control of Dynamic Systems*, 4th ed. USA: Prentice Hall PTR, 2001.

[28] H. Deng, J. Fang, Y. Qi, V. Debusschere, and Y. Tang, "Dynamic performance limitation and enhancement of grid-forming converters," in *2021 IEEE Energy Conversion Congress and Exposition (ECCE)*, Conference Proceedings, pp. 2979–2984.

[29] M. Ramezani, S. Li, F. Musavi, and S. Golestan, "Seamless transition of synchronous inverters using synchronizing virtual torque and flux linkage," *IEEE Transactions on Industrial Electronics*, pp. 1–1, 2019.

[30] T. QORIA, "Grid-forming control to achieve a 100power transmission systems," Thesis, 2020. [Online]. Available: https://pastel.archives-ouvertes.fr/tel-03078479

[31] X. Wang, Y. W. Li, F. Blaabjerg, and P. C. Loh, "Virtual-Impedance-Based Control for Voltage-Source and Current-Source Converters," *IEEE Transactions on Power Electronics*, vol. 30, no. 12, pp. 7019–7037, 2015.

[32] F. de Bosio, L. A. de Souza Ribeiro, F. D. Freijedo, M. Pastorelli, and J. M. Guerrero, "Effect of State Feedback Coupling and System Delays on the Transient Performance of Stand-Alone VSI With LC Output Filter," *IEEE Transactions on Industrial Electronics*, vol. 63, no. 8, pp. 4909–4918, 2016.

[33] E. Rodriguez-Diaz, F. D. Freijedo, J. C. Vasquez, and J. M. Guerrero, "Analysis and Comparison of Notch Filter and Capacitor Voltage Feedforward Active Damping Techniques for LCL Grid-Connected Converters," *IEEE Transactions on Power Electronics*, vol. 34, no. 4, pp. 3958–3972, 2019.

[34] X. Liu, Y. Qi, Y. Tang, Y. Guan, P. Wang, and F. Blaabjerg, "Unified Active Damping Control Algorithm of Inverter for LCL Resonance and Mechanical Torsional Vibration Suppression," *IEEE Transactions on Industrial Electronics*, vol. 69, no. 7, pp. 6611–6623, 2022.

[35] K. Jalili and S. Bernet, "Design of LCL Filters of Active-Front-End Two-Level Voltage-Source Converters," *IEEE Transactions on Industrial Electronics*, vol. 56, no. 5, pp. 1674–1689, 2009.

[36] L. Yun Wei, "Control and Resonance Damping of Voltage-Source and Current-Source Converters With LC Filters," *IEEE Transactions on Industrial Electronics*, vol. 56, no. 5, pp. 1511–1521, 2009.

[37] D. Pan, X. Ruan, C. Bao, W. Li, and X. Wang, "Optimized Controller Design for LCL-Type Grid-Connected Inverter to Achieve High Robustness Against Grid-Impedance Variation," *IEEE Transactions on Industrial Electronics*, vol. 62, no. 3, pp. 1537–1547, 2015.

[38] Y. He, X. Wang, X. Ruan, D. Pan, and K. Qin, "Hybrid Active Damping Combining Capacitor Current Feedback and Point of Common Coupling Voltage Feedforward for LCL-Type Grid-Connected Inverter," *IEEE Transactions on Power Electronics*, vol. 36, no. 2, pp. 2373–2383, 2021.

[39] X. Wang, F. Blaabjerg, and P. C. Loh, "Analysis and design of grid-current-feedback active damping for LCL resonance in grid-connected voltage source converters," in *2014 IEEE Energy Conversion Congress and Exposition (ECCE)*, Conference Proceedings, pp. 373–380.

Han Deng (Student Member, IEEE) received the B.Eng. degree in electrical engineering from Xi'an Jiaotong University, Xi'an, China, in 2017, and the M.Sc. degree in power engineering in 2018 from Nanyang Technological University, Singapore, where she is currently working toward the Ph.D. degree. Her research interests include modeling, stability analysis, and control of distributed generation in more-electronics power systems.

Jingyang Fang (Member, IEEE) received the B.Sc. and M.Sc. degrees in electrical engineering from Xi'an Jiaotong University, Xi'an, China, in 2013 and 2015, respectively, and the Ph.D. degree from School of Electrical and Electronic Engineering, Nanyang Technological University, Singapore, in 2019. From May 2018 to August 2018, he was a Visiting Scholar with the Institute of Energy Technology, Aalborg University, Aalborg, Denmark. From August 2018 to August 2019, he was a Research Fellow with School of Electrical and Electronic Engineering, Nanyang Technological University, Singapore. From August 2019 to August 2021, he was a Postdoctoral Researcher with the Duke University and TU Kaiserslautern. Since August 2021, he has joined School of Control Science and Engineering, Shandong University as a Full Professor. His research interests include power quality control, stability analysis and improvement, renewable energy integration, and digital control in more-electronics power systems. Dr. Fang is a recipient of the Humboldt Research Fellowship, two IEEE Prize Paper Awards, and one Best Presenter Award. He received the Chinese Government Award for Outstanding Self-Financed Students Abroad in 2018 and the Best Thesis Award from NTU in 2019. He was World's Top 2 % Highly Cited Scientists ranked by Stanford University.

Yang Qi (Member, IEEE) received the B.Sc. degree from Xi'an Jiaotong University, Xi'an, China, in 2016, and the Ph.D. degree from Nanyang Technological University, Singapore, in 2021, both in electrical engineering. He was a Visiting Student with Power Electronics, Microgrids, and Subsea Electrical Systems Center, in 2019. Since 2021, he has been with the School of Automation, Northwestern Polytechnical University as an Associate Professor. His research interests include modeling and control of power-electronics-based power systems. Dr. Qi was the recipient of the Doctoral Research Excellence Award from Nanyang Technological University, in 2021.

Yi Tang (Senior Member, IEEE) received the B.Eng. degree in electrical engineering from Wuhan University, Wuhan, China, in 2007, and the M.Sc. and Ph.D. degrees from the School of Electrical and Electronic Engineering, Nanyang Technological University, Singapore, in 2008 and 2011, respectively. From 2011 to 2013, he was a Senior Application Engineer with Infineon Technologies Asia Pacific, Singapore. From 2013 to 2015, he was a Postdoctoral Research Fellow with Aalborg University, Aalborg, Denmark. Since March 2015, he has been with Nanyang Technological University, where he is currently an Associate Professor. He is the Cluster Director of the Advanced Power Electronics Research Program with the Energy Research Institute, Nanyang Technological University. Dr. Tang was a recipient of the Infineon Top Inventor Award in 2012, the Early Career Teaching Excellence Award in 2017, the Best Associate Editor Award for IEEE Jounral of Emerging and Selected Topics in Power Electronics in 2018, the Outstanding Reviewer for the IEEE Transactions on Power Electronics in 2019, and four IEEE Prize Paper Awards. He is an Associate Editor for the IEEE Transactions on Power Electronics and the IEEE Jounral of Emerging and Selected Topics in Power Electronics.

Vincent Debusschere (Senior Member, IEEE) received the Ph.D. degree in ecodesign of electrical machines from the Ecole Normale Superieure de Cachan, Cachan, France, in 2009. In 2010, he joined the Electrical Engineering Laboratory, Grenoble Institute of Technology, Grenoble, France, as an Associated Professor. His research interests include renewable energy integration, modeling of flexibility levels for smart grids, multicriteria assessment, and optimal design of complex systems.